

Large negative magnetoresistance in the antiferromagnetic rare-earth dichalcogenide EuTe_2

Junjie Yin,¹ Changwei Wu,¹ Lisi Li,¹ Jia Yu,¹ Hualei Sun,¹ Bing Shen,¹
Benjamin A. Frandsen,² Dao-Xin Yao,¹ and Meng Wang^{1,*}

¹*School of Physics, Sun Yat-Sen University, Guangzhou 510275, China*

²*Department of Physics and Astronomy, Brigham Young University, Provo, Utah 84602, USA*



(Received 12 August 2019; revised manuscript received 9 December 2019; published 28 January 2020)

We report the synthesis and characterization of a rare-earth dichalcogenide EuTe_2 . An antiferromagnetic transition was found at $T_N = 11$ K. The antiferromagnetic order can be tuned by an applied magnetic field to access a first-order spin-flop transition and a spin-flip transition. These transitions are associated with a large negative magnetoresistance with a change of magnitude of resistivity over five orders. Magnetic susceptibility, heat capacity, and Hall coefficient measurements reveal that the moments of Eu^{2+} align along the c axis and holes are the majority carriers. Furthermore, density functional theory calculations demonstrate that the carriers near the Fermi surface mainly originate from the Te $5p$ orbitals and the magnetism is dominated by localized electrons from the Eu $4f$ orbitals. Our results suggest that EuTe_2 is an A -type antiferromagnetic material with large negative magnetoresistance.

DOI: [10.1103/PhysRevMaterials.4.013405](https://doi.org/10.1103/PhysRevMaterials.4.013405)

I. INTRODUCTION

The manipulation of the resistivity in magnetic or non-magnetic metals and semiconductors via the application of a magnetic field, i.e., magnetoresistance (MR), has attracted significant interest as a probe of fundamental physics and as a phenomenon with broad potential applications. The MR effect is frequently associated with insulator-metal transitions, spin-flop transitions, and spin-flip transitions in magnetic materials [1]. The mechanisms of the MR effect can be nontrivial and are often related to magnetic exchange interactions, Hund's couplings, and charge or orbital ordering. Notably, the giant MR (GMR) effect discovered in the magnetic multilayers of Fe/Cr in 1988 [2] has been widely applied in hard disks, magnetic memory chips, and many other spintronic devices. Colossal MR (CMR) effects have been found in doped manganese perovskites, but the requirements of a high magnetic field and low temperature have limited their practical applications [3]. Thus, the search for new MR systems with less stringent magnetic field and temperature requirements is important.

The CuAl_2 -type structure (AB_2) supports a variety of interesting physical properties and may be a good candidate for new MR materials. In this structure, each A atom is surrounded by eight B atoms [4]. The A atoms in the AB_2 compounds are normally divalent cations such as transition metals or rare-earth metals. The B atoms are generally the chalcogenides (S, Se, and Te) or antimony (Sb) and form $[B_2]^{2-}$ dimers stacking along the c axis, as in SrS_2 [5], BaTe_2 [6], EuSe_2 [7], and CrSb_2 [8,9]. Properties found in materials with this structure include superconductivity in the alloy $\text{CuAl}_{2.06}$ [10], thermoelectricity in $\text{Pb}(\text{Se}, \text{S})_2$ [11], and multiple magnetic transitions in EuSe_2 [7]. In the latter compound, the large magnetic moments of Eu^{2+} (spin $S = 7/2$) may

have a strong influence on the electronic properties. However, detailed studies on the magnetic and electronic properties of the Eu-based AB_2 system are still lacking.

In this paper, we report the synthesis and characterization of EuTe_2 , a CuAl_2 -type compound. By combining data from magnetic susceptibility, resistivity, heat capacity, Hall coefficient measurements, and density functional theory (DFT) calculations, we determine that EuTe_2 is a semiconductor with a small thermal activation gap. The magnetic moments on the Eu^{2+} cations order antiferromagnetically below $T_N = 11$ K. This magnetic order can be manipulated by an applied magnetic field, resulting in a large negative magnetoresistance which could be attributed to the change of the Fermi surface.

II. EXPERIMENT

Our measurements were performed on single-crystal samples of EuTe_2 . The single crystals were grown by the self-flux method, similar to EuTe_4 [12]. Eu (99.9%) and Te (99.999%) shots were combined in the molar ratio 1 : 10 and sealed in an evacuated quartz ampoule. The ampoule was slowly heated to 850 °C in 100 hours and held for 3 days, then slowly cooled to 450 °C in 300 hours followed by centrifuging at this temperature to separate crystals from the Te flux. Dark and shiny crystals were obtained and used in our experiments. Energy-dispersive x-ray spectroscopy (EDX) (EVO, Zeiss) was employed to determine the composition of the crystals. Single-crystal x-ray diffraction (XRD) measurements were conducted on a SuperNova (Rigaku) single-crystal x-ray diffractometer. The resistivity was measured using the standard four-probe method on single crystals with a typical size of $4 \times 1.5 \times 1$ mm³. The magnetic susceptibility and heat capacity were measured using a shaved single crystal with a size of $1 \times 1 \times 1$ mm³. All the transport measurements were conducted using a physical property measurement system (PPMS) (Quantum Design). The Vienna *ab initio* simulation package (VASP) was employed for the DFT calculations [13].

*wangmeng5@mail.sysu.edu.cn

TABLE I. Single-crystal refinement of EuTe_2 .

Empirical formula	EuTe_2
EDX formula	$\text{Eu}_1\text{Te}_{2.03}$
Formula weight	407.164
Temperature	150 K
Crystal system	Tetragonal
Space group	$I4/mcm$
Unit-cell parameters	$a = b = 6.9711(3) \text{ \AA}$ $c = 8.1800(5) \text{ \AA}$ $\alpha = \beta = \gamma = 90^\circ$
Atomic parameters	
Eu	$4a (1/2, 1/2, 1/4)$
Te	$8h (x, y, 1/2)$ $x = 0.6407(5), y = 0.8593(5)$
Volume Z	$397.52(3) \text{ \AA}^3$
Density	8.856 g/cm^3
Absorp. coeff.	29.906 mm^{-1}
$F(000)$	688
Crystal size (mm)	$0.15 \times 0.12 \times 0.02$
Crystal color	black
Radiation	$\text{Mo K}_\alpha (\lambda = 0.71073 \text{ \AA})$
2Θ for data collection	4.134° to 41.899°
Index ranges	$-13 \leq h \leq 9, -9 \leq k \leq 12,$ $-6 \leq l \leq 15$
Reflections collected	1330
Independent reflections	389
Data/restraints/parameters	389/0/7
Goodness-of-fit on F^2	1.021
Final R indexes [$I \geq 2\sigma(I)$]	$R_1 = 0.0360, wR_2 = 0.1210$
Final R indexes (all data)	$R_1 = 0.0375, wR_2 = 0.1233$
Large diff. peak/hole/ $e \text{ \AA}^{-3}$	$3.32 / -4.82$

III. RESULTS

A. Structure refinement

The average composition of our single crystals was determined by EDX to be $\text{EuTe}_{2.03}$, very close to a stoichiometric ratio of 1 : 2. We took several pieces of small single crystals for x-ray diffraction measurements. The refined results are consistent with a CuAl_2 -type structure, with the key results summarized in Table I. The space group is tetragonal $I4/mcm$ at 150 K, similar to its sister compound EuSe_2 [7]. The nearest-neighbor Eu^{2+} atoms are located along the c axis with a separation distance of 4.09 \AA . The Te atoms form $[\text{Te}_2]^{2-}$ dimers, which stack along the c axis. The c axis is somewhat elongated compared to the identical a and b axes. The crystal structure is illustrated in Fig. 1, together with various potential magnetic orders that will be subsequently discussed.

B. Resistivity

A voltage was applied along the c axis for all the resistivity measurements, which are summarized in Fig. 2. The data in Fig. 2(a) reveal clear semiconducting behavior. A fit of the thermal-activation gap was performed on the data from 30 to 300 K using the activation-energy model $\rho(T) = \rho_0 \exp(E_a/k_B T)$, where ρ_0 is a prefactor and k_B is the Boltzmann constant. The refined activation energy is $E_a = 16.24 \text{ meV}$. The resistivity has a value of $8.6 \times 10^3 \text{ } \Omega \text{ cm}$ at 1.8 K and decreases to $1.3 \times 10^{-1} \text{ } \Omega \text{ cm}$ at room temperature.

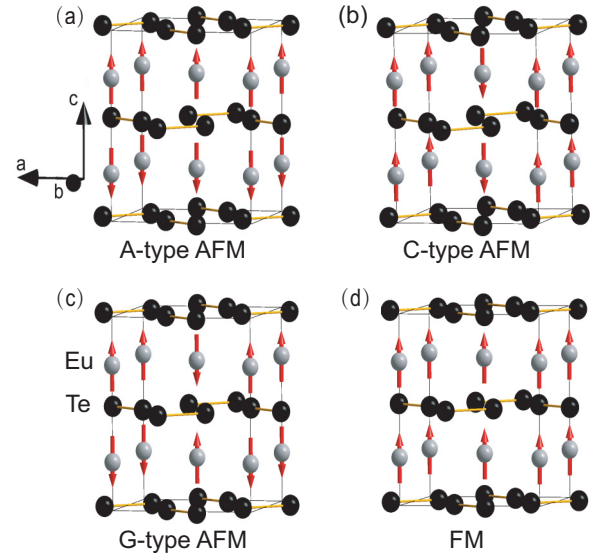


FIG. 1. Illustration of the crystal structure of EuTe_2 with four types of possible magnetic orders: (a) A-type antiferromagnetic order (AFM), (b) C-type AFM, (c) G-type AFM, and (d) ferromagnetic order. Eu atoms are white and Te atoms are black. The A-type AFM order has the lowest free energy.

To explore the influence of an applied magnetic field on the resistivity, we measured the transverse ($H \perp c$) and longitudinal ($H \parallel c$) MRs at 1.8 K under a field up to 14 T. Large negative MRs were observed at 1.8 K, as shown in Fig. 2(b). Scanning the field from 14 to -14 T and back in the $H \parallel c$ configuration results in hysteresis of the resistivity [right inset of Fig. 2(b)], evidencing a field-induced first-order transition associated with magnetism in this material. A similar phenomenon has been observed in $\text{Nd}_{0.5}\text{Sr}_{0.5}\text{MnO}_3$ [14]. The MR effect decreases as a function of temperature and is suppressed dramatically above T_N at 50 K [Fig. 2(c)].

The temperature dependence of the transverse and longitudinal MRs was investigated for fields of 0, 1, 2, 2.9, 5, and 10 T, as shown in Fig. 3. At 1.8 K, the resistivity decreases by five orders of magnitude under a field of 5 T compared to that with no applied field. This semiconductor-to-metal transition moves to a higher temperature and becomes broader under larger magnetic fields [15–17]. Interestingly, the resistivity shows an upturn at low temperatures, indicating a reentry to the semiconducting state. This is shown in the inset of Fig. 3(a). The semiconductor-to-metal and metal-to-semiconductor transition temperatures extracted from the resistivity measurements under magnetic fields have been summarized in Fig. 8. As seen in Fig. 3(b), the reentry of the semiconducting state at low temperatures when the field is applied along the b axis is not obvious at 2 T. However, the upturn of resistivity still exists below 8.4 K for 5 T. For the field of 10 T, the upturn of resistivity disappears as shown in the inset of Fig. 3(b).

C. Magnetic susceptibility

Magnetic susceptibility measurements as a function of temperature displayed in Figs. 4(a) and 4(b) reveal an antiferromagnetic (AFM) transition at $T_N = 11 \text{ K}$. The Curie-Weiss

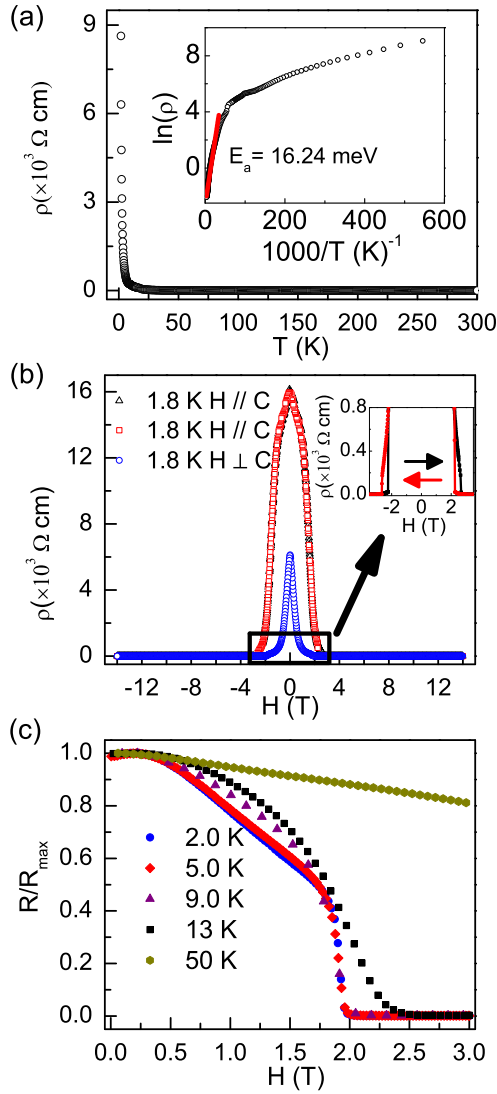


FIG. 2. (a) Temperature dependence of the resistivity in zero applied magnetic field. The red line in the inset shows a fit using the activation-energy model $\rho(T) = \rho_0 \exp(E_a/k_B T)$ (see main text for details). (b) Magnetic field dependence of the resistivity at $T = 1.8$ K with the field in the ab plane and the c axis. The data marked with black triangles were collected by scanning from negative to positive field, while the reverse order was used for the data marked with red squares. The inset on the right shows the hysteresis of the resistivity upon application and reversal of the magnetic field. (c) The normalized longitudinal MRs ($H \parallel c$) at 2, 5, 9, 13, and 50 K as a function of magnetic field.

law $\chi = C/(T - \theta)$ was employed to fit the susceptibility in the temperature range of 35–250 K, where C is the Curie constant and θ is the Curie-Weiss temperature. The fitting reveals an effective moment $\mu_{\text{eff}} = 7.5 \mu_B$ and $\theta = -6.05$ K. The effective moment μ_{eff} is very close to the theoretical expectation of $\mu = \sqrt{S(S+1)}g\mu_B = 7.9\mu_B$ for Eu^{2+} , where $g = 2$ is the spin Landau g factor of electrons and spin $S = 7/2$ is expected for Eu^{2+} . This negative θ agrees with the AFM transition below T_N . The field-direction dependence of the susceptibility at low temperatures indicates that the moments of the AFM order align along the c axis.

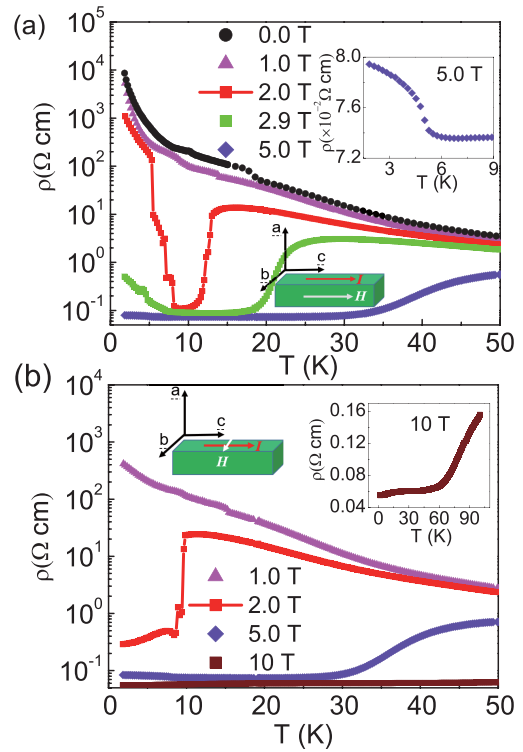


FIG. 3. (a) Resistivity as a function of temperature under magnetic fields of 0, 1, 2, 2.9, and 5 T parallel to the c axis. (b) Identical measurements as (a), using magnetic fields of 1, 2, 5, and 10 T parallel to the b axis. The insets in (a) and (b) show a closer view of the transitions at low temperatures and sketches of the geometry of the crystal and applied fields.

To further investigate the dependence of the susceptibility on the applied field, we performed isothermal magnetization (M) measurements as presented in Figs. 4(c) and 4(d). At 2 K, several obvious transitions could be observed in the magnetization in the case of the field applied along the c axis [Fig. 4(c)]. The abrupt increase at 3 T corresponds to a spin-flop transition of the AFM order. The magnetization saturates at $M_{\text{sat}} = 5.89 \mu_B$ per Eu^{2+} ion for magnetic fields above 7.6 T at 2 K, marking the spin-flip transition. The M_{sat} moment is smaller than that of the theoretical estimation, $M = gS \mu_B = 7.0 \mu_B$. This could be induced by the flux contaminated in the sample. With increasing temperature, the spin-flop and spin-flip transitions are weakened and finally vanish above T_N . The transition temperatures have been extracted and plotted in the $T - H$ phase diagram in Fig. 8. When the field is applied in the ab plane [Fig. 4(d)], the spin-flip transition dominates, while the spin-flop transition is not readily observable. The spin-flip field of 10 T for $H \perp c$ is larger than that of 7.6 T for $H \parallel c$, pointing to anisotropic magnetism in EuTe_2 . Small kinks could be observed in the $\partial M/\partial H$ curve in Fig. 4(d). The kinks may be caused by the imperfect alignment of the piece of single crystal. The transitions seen in the magnetization data in Fig. 4(c) are consistent with the MR transitions in Figs. 2(b) and 2(c), indicating that the large negative MR is related to the formation of the AFM order in EuTe_2 , as observed in $\text{Na}_{0.85}\text{CoO}_2$ [18], $\text{Ca}_{1-x}\text{Sr}_x\text{Co}_2\text{As}_2$ [19], and $\text{Ca}_{2-x}\text{Sr}_x\text{RuO}_4$ [20].

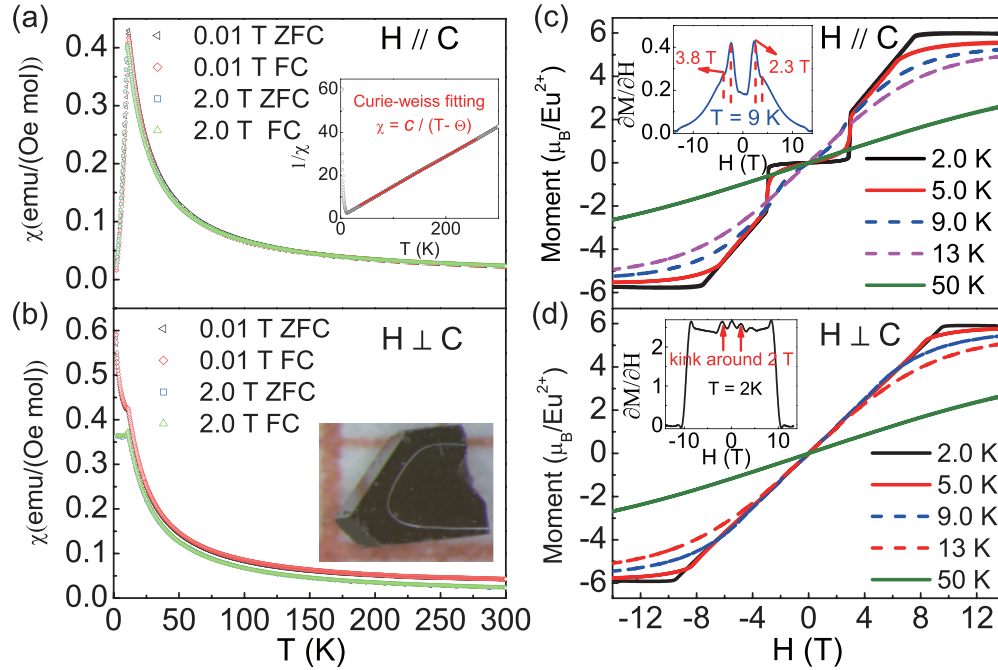


FIG. 4. Field-cooling (FC) and zero-field-cooling (ZFC) measurements of the magnetic susceptibility under fields of 0.01 and 2 T, (a) parallel to the c axis and (b) perpendicular to the c axis. The inset in (a) is a Curie-Weiss fit using the function $\chi = C/(T - \theta)$. (c),(d) Field-dependent magnetization at various temperatures with the field $H \parallel c$ (c) and $H \perp c$ (d) from 2 to 50 K. The insets in (c) and (d) are derivatives of the magnetization as a function of magnetic field.

D. Specific-heat capacity

In Fig. 5(a), we show the heat capacity measurements. A sharp λ -like transition occurs at $T_N = 11$ K, which is consistent with the AFM transition observed in the magnetic susceptibility measurements shown in Figs. 4(a) and 4(b). A model $C = \gamma T + nC_v$ was employed to fit the heat capacity, where $n = 3$ is the number of atoms in the chemical formula, $R = 8.314$ J/mol/K is the ideal gas constant, and $C_v = 9R(\frac{T}{\theta_D})^3 \int_0^{\theta_D/T} \frac{\xi^4 e^\xi}{(e^\xi - 1)^2} d\xi$ is the Debye model. γT and nC_v represent the contributions of electrons and phonons, respectively. A fitting in the range of 1.8–200 K yields $\gamma = 9.7$ mJ/mol/K² and $\theta_D = 165$ K. The small γ is consistent with the semiconducting ground state of EuTe_2 with $H = 0$.

To obtain the magnetic contribution to the heat capacity, we extrapolated and subtracted the electron and phonon contributions at low temperatures, as shown in Fig. 5(b). The magnetic entropy $S_m = \int_0^T \frac{C_{\text{mag}}}{T} dT$, is calculated to be 14.5 J/mol/K at $T_N = 11$ K, and saturates at 32 K with 17.28 J/mol/K, which is close to the theoretical value $R \ln(2S + 1)$ for Eu^{2+} . The increase of S_m between 11 and 32 K could be attributed to the contribution of the spin fluctuations.

E. Hall coefficient

In order to obtain the type and density of the carriers in EuTe_2 , we conducted Hall measurements with field from -1 to 1 T at temperatures of 4, 10, 15, 20, 50, and 100 K. The voltage was applied along the c axis and the field was perpendicular to the c axis. The single crystal we used was shaved as thin as possible to reduce the MR effect. The Hall resistivity ρ_{xy} was obtained from $(\rho_{xy}^{+H} - \rho_{xy}^{-H})/2$, where

$\rho_{xy}^{\pm H}$ are ρ_{xy} measured with positive and negative magnetic fields, respectively. The ρ_{xy} is linear and has positive slopes at temperatures above T_N , as shown in Fig. 6(a), which demonstrates that the majority carriers are holes. Accordingly, we calculated the carrier density n_h based on one type of carrier model. The results are plotted in 6(b). The carrier density n_h decreases slightly below T_N , then increases above T_N as a function of temperature. The change of n_h indicates that the magnetic order interplays with the Fermi surface. Similar behavior has also been observed in $\text{TaFe}_{1+y}\text{Te}_3$ [21,22].

F. DFT calculations

To investigate the magnetic structure of EuTe_2 , DFT calculations have been performed to compare the free energies of four magnetic structures, as illustrated in Fig. 1. The calculated free energies for A -type, C -type, and G -type AFM orders, and ferromagnetic (FM) order, are -58.5270 , -58.5209 , -58.4557 , and -58.1396 eV, respectively. The A -type AFM order therefore has the lowest predicted energy. The orientations of the moments are also investigated by implementing spin-orbital coupling (SOC). The energy of the moments along the c axis is 2.503 meV/Eu lower than that of the moments along the a and b axes. Consistent with the magnetic susceptibility measurements, the DFT calculations suggest that the A -type AFM order with moments aligning along the c axis is most likely the magnetic ground state.

In addition, we calculated the electronic density of states with A -type AFM order in Fig. 7. To account for electronic correlation effects, the on-site Coulomb interaction U was introduced. The impact of U on the electronic structure was investigated using values of U ranging from 0 to 8 eV. EuTe_2

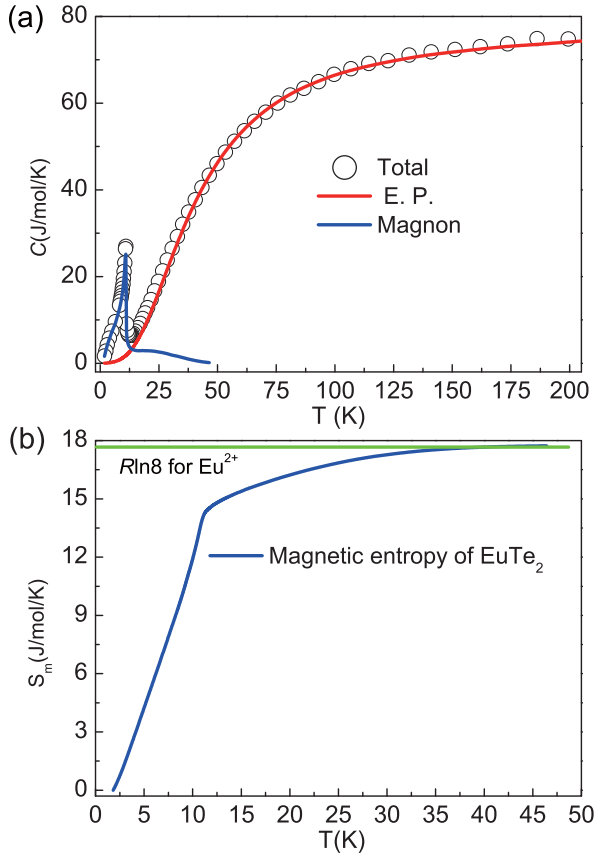


FIG. 5. (a) Heat capacity of EuTe_2 as a function of temperature. The red line shows a fit with the contributions from electron and phonon (E. P.) to the heat capacity using $C = \gamma T + nC_v$. The blue line represents the extracted magnetic contribution. (b) The magnetic entropy of Eu^{2+} and a theoretical value ($R\ln 8$) for Eu^{2+} .

is metallic for $U = 0$. The experimentally observed magnitude of the activation gap $E_a = 16.24$ meV is reproduced with $U = 6$ eV, where the calculated $E_a = 14.6$ meV. Hence, we used $U = 6$ eV for Eu^{2+} in our subsequent calculations. The results without including the SOC are summarized in Fig. 7, indicating that localized Eu $4f$ electrons reside ~ 2 eV below the Fermi level and support the localized magnetic moments, while the Te $5p$ orbitals are more spread out in energy and make a weak contribution to the density of states at the Fermi level.

The electronic structure for the spin-flipped state is also investigated in the calculation with fixing $U = 6$ meV and FM order. In the FM state, the Te $5p$ orbital is lifted and crosses the Fermi surface, yielding a metallic state that is consistent with our experimental result. Hence, the large MR could be related to the change of the Fermi surface in the spin-flipped state induced by the magnetic field.

IV. DISCUSSION AND SUMMARY

The results presented here reveal rich temperature- and field-dependent phase behavior in EuTe_2 . This is summarized by the $T - H$ phase diagram in Fig. 8. The semiconductor-to-metal transition temperatures were extracted from the resistivity measurements, while the antiferromagnetic, spin-flop,

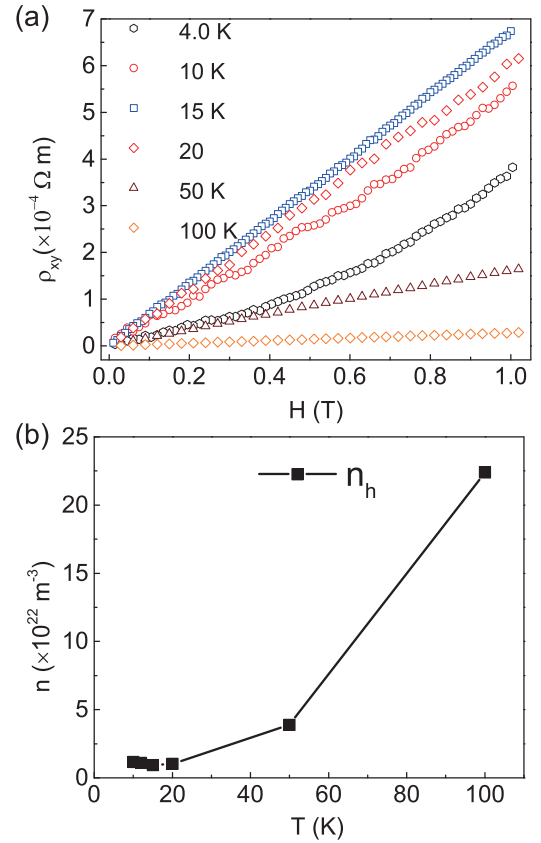


FIG. 6. (a) Hall resistivity of EuTe_2 at 4, 10, 15, 20, 50, and 100 K. (b) Extracted carrier density n_h at the temperatures presented in (a). n_h decreases below T_N , then turns up above T_N .

and spin-flip transitions were extracted from the magnetic susceptibility measurements with the field applied parallel to the c axis (and, therefore, also parallel to the ordered moments). The whole $T - H$ phase diagram can be divided into a semiconducting region and a metallic region based on conductance. Below $T_N = 11$ K, we observe an AFM region, a spin-flop transition region showing field-induced hysteresis, and a saturated spin-flip region. The details of these magnetic states and transitions are governed by the relative coupling strengths of the antiferromagnetic exchange interaction, easy-axis anisotropy, and uniaxial single-ion anisotropy to the magnetic field, consistent with the expectations from mean-field theory [23]. The reentrant semiconducting region for fields $\sim 2-8$ T largely coincides with the spin-flip transition region, suggesting the interactions between the localized $4f$ electrons of Eu and the itinerant $5p$ electrons of Te.

The semiconductor-to-metal and metal-to-semiconductor transitions in EuTe_2 directly couple to the metamagnetic transition. This behavior could be interpreted by the competitions between the thermal fluctuations, magnetic exchange interactions, easy-axis anisotropy, and the magnetic torques of the magnetic field to the local moments. In addition, the resistivity increases rapidly when the system enters into the AFM state, which can be attributed to the opening of an electronic gap, while the applied magnetic fields change the Fermi surface and induce a metallic state in EuTe_2 . Thus, the resistance becomes much smaller. However, the large negative

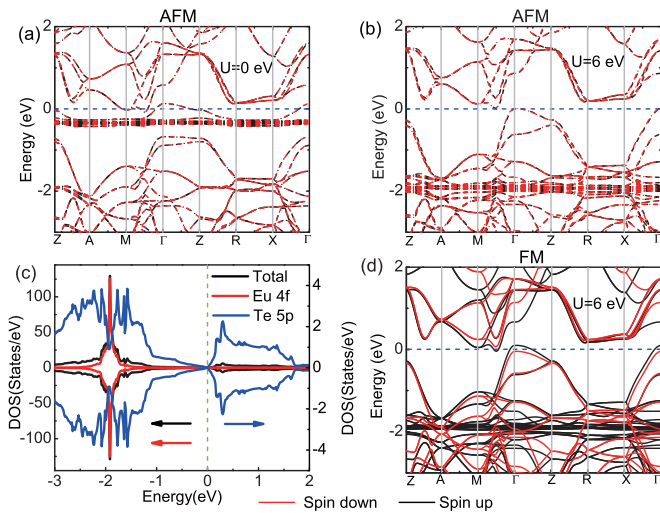


FIG. 7. DFT calculations of the band structures with AFM order and (a) $U = 0$, (b) $U = 6$ eV. The band gap for $U = 6$ eV is 14.6 meV. (c) Density of states (DOS) for (b) with orbital characters of the electrons in EuTe_2 . (d) A DFT calculation of the band structure with FM order and $U = 6$ eV to simulate the spin-flipped state.

magnetoresistance is merely observed in bulk compounds. The value of the negative MR of nearly -100% [defined by $(\rho_H - \rho_0)/\rho_0$] at 2 K and $H = 3$ T is larger than that of the TiTeI nanosheets (-85%) [24], Fe/Cr/Fe heterostructure (-60%) [2], and perovskitelike La-Ba-Mn-O magnetic thin film (-60%) [25].

In summary, we have successfully synthesized and characterized a rare-earth dichalcogenide system EuTe_2 . By combining structural refinements, resistivity, magnetic susceptibility, specific-heat capacity, and DFT calculations, we demonstrate that EuTe_2 exhibits antiferromagnetic order, most likely of the A type, which can be easily tuned with a magnetic field. Large negative magnetoresistance that couples with the magnetic

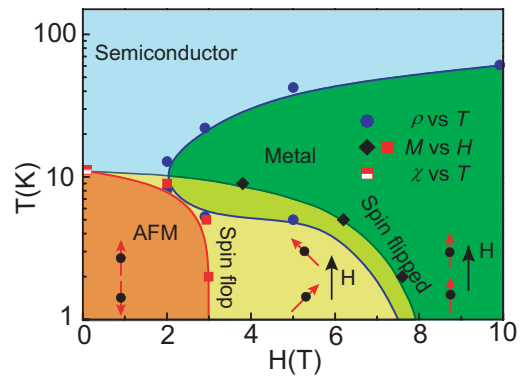


FIG. 8. A proposed $T - H$ phase diagram for EuTe_2 . The sample undergoes a transition from a semiconducting state to a metallic state by applying a magnetic field. The metallic region is shaded green. Below the AFM transition temperature T_N , the spins flop at around 3 T and cannot progress as the magnetic field increases until flipped, as marked by the black diamonds.

states is observed. Our work opens up prospects to look for negative magnetoresistance in Eu -based magnetic materials.

ACKNOWLEDGMENTS

M.W. is thankful for fruitful discussions with Shiliang Li and Haifeng Li. The research was supported by Grant No. NSFC-11904414 and by NSF of Guangdong under Contract No. 2018A030313055, the Hundreds of Talents program of Sun Yat-Sen University, and Young Zhujiang Scholar program. H.L.S. was supported by Grant No. NSFC-11904416 and the Fundamental Research Funds for the Central Universities (Grant No. 18lgy73). C.W. and D.X.Y. acknowledge support from Grants No. NKRDP-2018YFA0306001, No. NKRDP-2017YFA0206203, No. NSFC-11574404, the National Supercomputer Center in Guangzhou, and the Leading Talent Program of Guangdong Special Projects.

- [1] E. Dagotto, T. Hotta, and A. Moreo, *Phys. Rep.* **344**, 0012117 (2001).
- [2] F. N. Van Dau, *Phys. Rev. Lett.* **61**, 2472 (1988).
- [3] M. Uehara, S. Mori, C. H. Chen, and S.-W. Cheong, *Nature (London)* **399**, 560 (1999).
- [4] E. E. Havinga, H. Damsma, and P. Hokkelling, *J. Less-Common Met.* **27**, 169 (1972).
- [5] I. Kawada, K. Kato, and S. Yamaoka, *Acta Crystallogr. Sect. B* **32**, 3110 (1976).
- [6] J. Li, H. Guo, J. R. Carey, S. Mulley, D. M. Proserpio, and A. Sironi, *Mater. Res. Bull.* **29**, 1041 (1994).
- [7] J. A. Aitken, J. A. Cowen, and M. G. Kanatzidis, *Chem. Mater.* **10**, 3928 (2002).
- [8] B. C. Sales, A. F. May, M. A. McGuire, M. B. Stone, D. J. Singh, and D. Mandrus, *Phys. Rev. B* **86**, 235136 (2012).
- [9] Y. Y. Jiao, Z. Y. Liu, M. A. McGuire, S. Calder, J.-Q. Yan, B. C. Sales, J. P. Sun, Q. Cui, N. N. Wang, Y. Sui, Y. Uwatoko, B. S. Wang, X. L. Dong, and J.-G. Cheng, *Phys. Rev. Mater.* **3**, 074404 (2019).
- [10] E. E. Havinga, *J. Less-Common Met.* **27**, 187 (1972).
- [11] D. Ni, S. Guo, K. M. Powderly, R. Zhong, J. Lin, T. Kong, F. Alex Cevallos, and R. J. Cava, *J. Solid State Chem.* **269**, 442 (2019).
- [12] D. Wu, Q. M. Liu, S. L. Chen, G. Y. Zhong, J. Su, L. Y. Shi, L. Tong, G. Xu, P. Gao, and N. L. Wang, *Phys. Rev. Mater.* **3**, 024002 (2019).
- [13] G. Kresse and J. Hafner, *Phys. Rev. B* **47**, 558 (1993).
- [14] H. Kuwahara, Y. Tomioka, A. Asamitsu, Y. Moritomo, and Y. Tokura, *Science* **270**, 961 (1995).
- [15] Y. Tokura, A. Urushibara, Y. Moritomo, T. Arima, A. Asamitsu, G. Kido, and N. Furukawa, *J. Phys. Soc. Jpn.* **63**, 3931 (1994).
- [16] W. Felsch and K. Winzer, *Solid State Commun.* **13**, 569 (1973).
- [17] S. Malick, D. Das, and Z. Hossain, *J. Magn. Magn. Mater.* **482**, 108 (2019).
- [18] J. L. Luo, N. L. Wang, G. T. Liu, D. Wu, X. N. Jing, F. Hu, and T. Xiang, *Phys. Rev. Lett.* **93**, 187203 (2004).
- [19] J. J. Ying, Y. J. Yan, A. F. Wang, Z. J. Xiang, P. Cheng, G. J. Ye, and X. H. Chen, *Phys. Rev. B* **85**, 214414 (2012).

- [20] S. Nakatsuji, D. Hall, L. Balicas, Z. Fisk, K. Sugahara, M. Yoshioka, and Y. Maeno, *Phys. Rev. Lett.* **90**, 137202 (2003).
- [21] R. H. Liu, M. Zhang, P. Cheng, Y. J. Yan, Z. J. Xiang, J. J. Ying, X. F. Wang, A. F. Wang, G. J. Ye, X. G. Luo *et al.*, *Phys. Rev. B* **84**, 184432 (2011).
- [22] N. F. Mott, *Philos. Mag.* **30**, 403 (1974).
- [23] H.-F. Li, *npj Comput. Mater.* **2**, 16032 (2016).
- [24] Y. Guo, J. Dai, J. Zhao, C. Wu, D. Li, L. Zhang, W. Ning, M. Tian, X. C. Zeng, and Y. Xie, *Phys. Rev. Lett.* **113**, 157202 (2014).
- [25] R. von Helmolt, J. Wecker, B. Holzapfel, L. Schultz, and K. Samwer, *Phys. Rev. Lett.* **71**, 2331 (1993).